Pattern selection in Rayleigh-Bénard convection with nonlinear viscoelastic fluids

Xin Zheng ⓘ, Fouad Hagani, M'hamed Boutaous ⓘ,* Ronnie Knikker, and Shihe Xin
*Université Lyon, CNRS, INSA-Lyon, Université Claude Bernard Lyon 1, CETHIL UMR5008,
F-69621 Villeurbanne Cedex, France*

Dennis A. Siginer
*Centro de Investigación en Creatividad y Educación Superior and Departamento de Ingeniería Mecánica,
Universidad de Santiago de Chile, 8320000 Santiago, Chile*

Rayleigh-Bénard convection in a rectangular enclosure of aspect ratio 2:1 filled by a class of nonlinear viscoelastic fluids represented by the Phan-Thien–Tanner (PTT) constitutive equation is investigated numerically. Governing equations are discretized by finite-difference methods in space and time. The momentum and PTT constitutive equations are written in a quasilinear formulation. Quasilinear terms are treated with the high-order upwind central (HOUC) method and velocity-pressure coupling is handled through the projection method. The developed model is validated for Oldroyd-B types of working fluids. The onset of time-dependent convection is observed and the critical Rayleigh number is determined for PTT types of fluids. The time-dependent flow pattern transition is investigated and explained. A transition from time-dependent flow to steady-state flow is observed at a higher Rayleigh number and the corresponding critical Rayleigh number is computed. The effect of the rheological parameters on heat transfer is investigated.
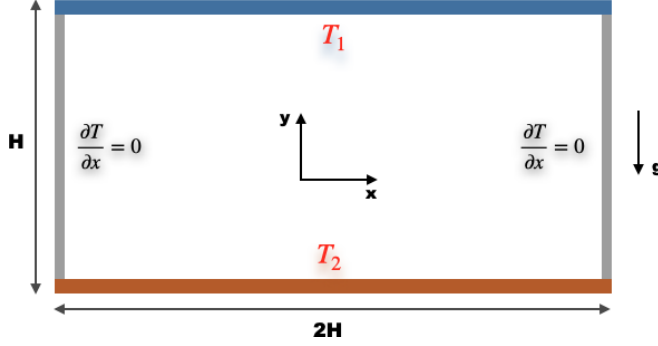
I. INTRODUCTION

Pattern selection at the startup of Rayleigh-Bénard convection (RBC) with Newtonian fluids has been studied extensively numerically and experimentally. However, RBC studies with viscoelastic fluids are few compared to RBC investigations with Newtonian fluids. Thus, there is a need for further in-depth investigations of the RBC with nonlinear viscoelastic fluids as applications both present and emerging abound in industry and nature. Some examples are chemical and manufacturing processes and convection in the Earth's mantle. Several aspects of this physical phenomenon are still not yet elucidated. RBC is complicated enough by its very nature without additional difficulties introduced by the nonlinear constitutive construct of the viscoelastic fluid with additional material parameters such as relaxation and retardation times as well as the degree of elasticity embedded in the fluid. Given the compounded difficulties, a numerical approach is best suited to tackle this problem. A major difficulty in numerical simulations of the flow of viscoelastic fluids is the instability caused by the increasing inertia and elasticity of the fluid independently of the discretization chosen, called in the literature the high Weissenberg number problem. Linear stability analysis predicts the critical Rayleigh number at which thermal convection starts whereas the magnitude of the convection amplitude is determined by the nonlinear stability analysis [1]. Linear and nonlinear stability analyses in the literature provide evidence that many parameters have

---

*mhamed.boutaous@insa-lyon.fr

a huge impact on the critical Rayleigh number and convection flow pattern. The earliest linear and nonlinear stability analyses of the RBC with Newtonian fluids were conducted by Chandrasekhar [2] and Malkus and Veronis [3]. The first linear stability analysis for RBC with viscoelastic fluids was published in 1968 by Green [4], who used an upper convected Maxwell model with a single relaxation time to characterize the fluid and to describe the onset of convection in a thin fluid layer heated from below to establish the conditions under which an oscillating convection instability may appear. This was followed by Vest and Arpaci [5] and Sokolov and Tanner [6], who expanded the investigation of this intriguing phenomenon to the oscillating mode of instability which appears when the ratio of viscoelastic relaxation time to thermal relaxation time is high with the thermal relaxation time defined by d^2/κ, where d is the thickness of the viscoelastic fluid layer and κ is the thermal diffusivity.

Nonlinear stability analysis of the RBC with viscoelastic fluids has been a focus of attention by several investigators in the following decades, some of them of quite recent memory: Eltayeb [7], Rosenblat [8], Renardy and Renardy [9], Martinez-Mardones and Perez-Garcia [10,11], Park and Lee [12,13], Park and Ryu [14], Park and Park [15], and Park [16]. In their contributions, the relationship between viscoelastic parameters and the critical Rayleigh number reflecting the flow mode instability that is the flow pattern transition from stationary convection to oscillating convection was further investigated in depth and illustrated. Relatively more sophisticated viscoelastic constitutive models were used in these studies as compared to the basic upper-convected Maxwell model used much earlier in the pioneering work of Green [4]. The heating and cooling boundary conditions used ranged from the rigid-free condition with a free surface to the rigid-rigid (solid wall) condition. Most of the research works outlined above focused on periodic boundary conditions and/or an infinite plane, which can be approximated by a one-dimensional instability analysis. This treatment also limits the application of the stability analysis as the boundary conditions have a significant effect on the flow and heat transfer in the Rayleigh-Bénard convection. The first linear and nonlinear instability analysis of the Rayleigh-Bénard convection with viscoelastic fluids in an enclosed cavity with an aspect ratio (A) different than one ($A \in [1, 10]$) was conducted by Park and Ryu [14]. They used a Chebyshev pseudospectral method coupled with a general viscoelastic constitutive model which encompasses Maxwell, Oldroyd, and Phan-Thien–Tanner (PTT) models. The effects of the Weissenberg number We and β (ratio of solvent viscosity μ_s to total viscosity $\mu_0 = \mu_s + \mu_p$, where μ_p is the molecular viscosity at zero shear rate) on the critical Rayleigh number for convection startup as well as convection cell structure and formation with different aspect ratios were studied. Park and Ryu [14] also investigated flow pattern selection mechanisms at different We and β, with aspect ratios $A = 2.0$ and 6.0. They determine that the critical Rayleigh number decreases as the Weissenberg number We increases and/or β decreases. Flow pattern selection is also strongly dependent on the parameters We and β. The stability exchange criteria derived are only valid when a new flow pattern grows monotonically without oscillation [13]. If the flow pattern grows with oscillation, the instability is called overstability. As We increases and/or β decreases, the startup convection flow pattern will be in the overstability mode, otherwise the convection will be steady, as demonstrated by Park and Ryu [1]. Park and Park [15] and Park [16] also numerically simulated the Rayleigh-Bénard convection with a PTT model to shows that the time period of local vorticity intensity is almost two times larger than that of local momentum with growing values of β.

To our knowledge, the way the flow pattern transition happens from time-periodic reversal convection to the next flow pattern (turbulence or other) needs to be numerically and experimentally investigated. In this paper, a direct numerical simulation model with a quasilinear treatment of the convective terms in the momentum equation and a viscoelastic constitutive equation representing a class of nonlinearly viscoelastic fluids are employed to solve the Rayleigh-Bénard problem. The Phan-Thien–Tanner constitutive model is singled out of this class. It has two more material parameters than the Oldroyd-B constitutive model, ϵ and ξ. The former material parameter ϵ is linked to the elongational behavior of the nonlinearly viscoelastic fluid, and the latter material parameter ξ is related to the slip behavior between long molecular chains in the solvent and the solvent itself. The effect of material parameters ϵ, ξ, β and the parameter We on the flow structure

FIG. 1. Computational configuration of aspect ratio $A = 2$.

and heat transfer were examined in the paper when the startup convection flow pattern is in the overstability region. We introduce a second critical Rayleigh number, which describes the transition of the flow pattern from time-periodic oscillating flow to steady flow and investigate the influence of the material parameters on this second critical Rayleigh number.

II. COMPUTATIONAL MODEL

The Rayleigh-Bénard convection is simulated in a 2:1 cavity filled with a nonlinear viscoelastic fluid (Fig. 1). In the Cartesian coordinate system, x is the horizontal direction perpendicular to g (gravity), and y denotes the vertical direction parallel to g. A temperature difference $\Delta T = (T_2 - T_1)$ is imposed between two horizontal walls with $T_2 > T_1$ representing the temperatures on the lower and upper walls, respectively. Vertical walls are adiabatic. Adopting the incompressible Boussinesq approximation, the governing field equations read as follows:.

$$\nabla \cdot \boldsymbol{u} = 0, \tag{1}$$

$$\rho_0 \left(\frac{\partial \boldsymbol{u}}{\partial t} + (\boldsymbol{u} \cdot \nabla) \right) \boldsymbol{u} = -\nabla p + \nabla \cdot \boldsymbol{\sigma} - \rho_0 [1 - \alpha (T - T_0)] g \boldsymbol{e_j}, \tag{2}$$

$$\frac{\partial T}{\partial t} + (\boldsymbol{u} \cdot \nabla) T = \frac{k}{\rho_0 C_p} \Delta T + 2\mu_s \boldsymbol{D} : \nabla \boldsymbol{u} + \boldsymbol{\tau_p} : \nabla \boldsymbol{u}, \tag{3}$$

where $\boldsymbol{u} = (u_1, u_2)$ stands for the velocity vector in the two-dimensional (2D) flow field with u_1 and u_2 representing the velocity components in the x and y directions, respectively. p, T, g, ρ_0, k, and C_p stand for the pressure, the temperature, the gravitational acceleration, the liquid density at the temperature $T_0 = \frac{T_2 + T_1}{2}$, the thermal conductivity, and the specific heat, respectively. $\boldsymbol{e_j}$ is the unit vector in the vertical direction and the α stands for the coefficient of heat expansion. The last term of Eq. (2) represents the Oberbeck-Boussinesq approximation. The second and third terms on the right-hand side (RHS) of Eq. (3) are the viscous dissipation and elastic dissipation terms leading to the temperature rise in the flow. Their importance in RBC flow will be discussed. The total stress $\boldsymbol{\sigma}$ is the sum of the contributions from the Newtonian solvent $\boldsymbol{\tau_s}$ and from the embedded polymeric long chain molecules $\boldsymbol{\tau_p}$, respectively, $\boldsymbol{\sigma} = \boldsymbol{\tau_s} + \boldsymbol{\tau_p}$. The solvent contribution $\boldsymbol{\tau_s} = \mu_s \boldsymbol{D}$ is well known, where $\boldsymbol{D} = \frac{1}{2}(\nabla \boldsymbol{u} + \nabla \boldsymbol{u}^T)$ is the rate of deformation tensor and μ_s is the solvent viscosity. The polymeric contribution to the total stress, $\boldsymbol{\tau_p}$, is the molecular contributed extra-stress tensor given by the nonlinear viscoelastic constitutive equation. $\boldsymbol{\tau_p}$ is governed by the PTT constitutive model,

$$\overset{\nabla}{\boldsymbol{\tau_p}} = \frac{\partial \boldsymbol{\tau_p}}{\partial t} + (\boldsymbol{u} \cdot \nabla) \boldsymbol{\tau_p} - \nabla \boldsymbol{u}^T \cdot \boldsymbol{\tau_p} - \boldsymbol{\tau_p} \cdot \nabla \boldsymbol{u}, \tag{4}$$

$$\overset{\nabla}{\boldsymbol{\tau_p}} = -\frac{1}{\lambda} \boldsymbol{\tau_p} + 2\frac{\mu_p}{\lambda} \boldsymbol{D} + a \left[-\frac{\epsilon}{\mu_p} \mathrm{tr}(\boldsymbol{\tau_p}) \boldsymbol{\tau_p} - \xi (\boldsymbol{D} \boldsymbol{\tau_p} + \boldsymbol{\tau_p} \boldsymbol{D}) \right], \tag{5}$$

where λ is the relaxation time, and μ_p is the polymer viscosity at zero shear rate.

The following scale factors are introduced to nondimensionalize the governing field equations,

$$x^* = \frac{x}{H}, \quad t^* = t\frac{U_c}{H}, \quad \boldsymbol{u^*} = \frac{\boldsymbol{u}}{U_c}, \quad T^* = \frac{T - T_0}{T_2 - T_1}, \quad p^* = \frac{p}{\rho_0 U_c^2}, \quad \text{and} \quad \boldsymbol{\tau_p^*} = \frac{\boldsymbol{\tau_p}}{\rho U_c^2},$$

with H the cavity height, $T_0 = \frac{T_2 + T_1}{2}$, and the reference velocity $U_c = \frac{\kappa}{H}\sqrt{\text{Ra}}$. Here, Ra is the Rayleigh number defined as

$$\text{Ra} = \frac{\alpha g \Delta T H^3}{\nu \kappa}, \tag{6}$$

where $\kappa = \frac{k}{\rho_0 C_p}$ is the thermal diffusivity and ν is the kinematic viscosity of the working fluid. In order to simplify the notation, hereafter we drop the asterisk (*) from all the dimensionless variables. The dimensionless governing equations are then written as

$$\boldsymbol{\nabla} \cdot \boldsymbol{u} = 0, \tag{7}$$

$$\frac{\partial \boldsymbol{u}}{\partial t} + (\boldsymbol{u} \cdot \boldsymbol{\nabla})\boldsymbol{u} = -\nabla p + \beta \frac{\text{Pr}}{\sqrt{\text{Ra}}}\boldsymbol{\Delta u} + \boldsymbol{\nabla} \cdot \boldsymbol{\tau_p} + \text{Pr}\, T \boldsymbol{e_j}, \tag{8}$$

$$\overset{\triangledown}{\boldsymbol{\tau_p}} + \frac{\boldsymbol{\tau_p}}{\text{We}\sqrt{\text{Ra}}} - 2\frac{1 - \beta}{\text{Ma}^2}\boldsymbol{D} = A\left[-\epsilon\frac{\sqrt{\text{Ra}}}{(1 - \beta)\text{Pr}}\text{tr}(\boldsymbol{\tau_p})\boldsymbol{\tau_p} - \xi(\boldsymbol{D\tau_p} + \boldsymbol{\tau_p D})\right], \tag{9}$$

$$\frac{\partial T}{\partial t} + (\boldsymbol{u} \cdot \boldsymbol{\nabla})T = \frac{1}{\sqrt{\text{Ra}}}\boldsymbol{\Delta}T + 2\beta\frac{\text{Ec}\,\text{Pr}}{\sqrt{\text{Ra}}}\boldsymbol{D} : \boldsymbol{\nabla u} + \text{Ec}\,\boldsymbol{\tau_p} : \boldsymbol{\nabla u}, \tag{10}$$

where $\beta = \frac{\mu_s}{\mu_0}$ is the ratio of solvent viscosity to total viscosity $\mu_0 = \mu_s + \mu_p$, $\text{Pr} = \frac{\mu_0 C_p}{k}$ is the Prandtl number, $\text{We} = \frac{\lambda\kappa}{H^2}$ the Weissenberg number, and $\text{Ma} = \sqrt{\text{Ra}\,\text{We}/\text{Pr}}$ the Mach number. The latter gives the ratio of the shear wave speed to the characteristic velocity of the fluid. In Eq. (10), the dimensionless Eckert number Ec expresses the relationship between the kinetic energy and the enthalpy, and is used to characterize the extent of the influence of heat dissipation:

$$\text{Ec} = \frac{U_c^2}{C_p \Delta T}. \tag{11}$$

When Ec assumes a small value ($\ll 1$), the effects of the viscous dissipation can be neglected. For all the cases investigated in this work, Ec takes on values of the order of $O(10^{-10})$, and the magnitude of the values of $\beta\frac{\text{Ec}\,\text{Pr}}{\sqrt{\text{Ra}}}$ corresponds to $O(10^{-11})$. Therefore, viscous dissipation and elastic dispersion are ignored in the calculations presented in this paper.

We point out that due to the definition of the reference velocity $U_c = \frac{\kappa}{H}\sqrt{\text{Ra}}$ in this paper, the natural way to define We is to use U_c as has been done by Cheng *et al.* [17]. The drawback of using U_c to define We is that We will now change with Rayleigh number. In this paper a definition of We independent of Ra, $\text{We} = \kappa\lambda/H^2$, is adopted. For example, for Ra = 1600 and We = 0.1 in the present work the equivalent Weissenberg number is We = 10.58 in the work by Cheng *et al.* [17] (in their work $U_c = \sqrt{\alpha g H \Delta T}$).

The dimensionless problem is defined on the computational domain Ω: $(x, y) \in [0, 2] \times [0, 1]$. The velocity boundary conditions are no slip and the thermal boundary conditions are adiabatic on the vertical walls and isothermal on the horizontal walls:

    (1) at $y = 0$: $u_1 = u_2 = 0$, $T = 1/2$;
    (2) at $y = 1$: $u_1 = u_2 = 0$, $T = -1/2$;
    (3) at $x = 0, 2$: $u_1 = u_2 = 0$, $\frac{\partial T}{\partial x} = 0$.

III. NUMERICAL ALGORITHM

A. Quasilinear formulation

To simplify the numerical process, we firstly reorganized Eqs. (8) and (9) into a quasilinear system by separating the homogeneous part and the source term,

$$\frac{\partial W}{\partial t} + \sum_{i=1}^{2} A_i \frac{\partial W}{\partial x_i} = S_{\text{ql}}, \tag{12}$$

where $W = [u_1, u_2, \tau_{11}, \tau_{12}, \tau_{22}]$ is the vector of variables and includes velocity components u_i and extra-stress components τ_{ij}. S_{ql}, the source term, includes pressure, buoyancy, and viscous terms of the momentum equation and feature terms of the PTT constitutive equation and is written as

$$S_{\text{ql}} = \begin{bmatrix} -\nabla p + \beta \frac{\text{Pr}}{\sqrt{\text{Ra}}} \Delta \boldsymbol{u} + \text{Pr}\, T \boldsymbol{e}_j \\ \frac{-\tau_p}{\text{We}\sqrt{\text{Ra}}} - A\left[\frac{\epsilon\sqrt{\text{Ra}}}{(1-\beta)\text{Pr}} \text{tr}(\boldsymbol{\tau}_p)\boldsymbol{\tau}_p + \xi(\boldsymbol{D}\boldsymbol{\tau}_p + \boldsymbol{\tau}_p\boldsymbol{D})\right] \end{bmatrix}. \tag{13}$$

A_i is the matrix acting on the first derivative of W in the direction i. For example, A_1 is expressed as

$$A_1 = \begin{bmatrix} u_1 & 0 & -1 & 0 & 0 \\ 0 & u_1 & 0 & -1 & 0 \\ -2\left(\frac{1-\beta}{\text{Ma}^2} + \tau_{11}\right) & 0 & u_1 & 0 & 0 \\ -\tau_{12} & -\left(\frac{1-\beta}{\text{Ma}^2} + \tau_{11}\right) & 0 & u_1 & 0 \\ 0 & -2\tau_{12} & 0 & 0 & u_1 \end{bmatrix}. \tag{14}$$

In simple shear flow with an Oldroyd-B constitutive model, the system is hyperbolic only when $(\tau_{ii} + \frac{1-\beta}{\text{Ma}^2})$ is positive for each i [18,19]. To reveal the hyperbolic feature of our quasilinear governing system, the real spectra of A_i need to be satisfied. Symbolic computation of the eigenvalues and eigenvectors of A_i shows that the eigenvalues of A_i depend on $(\sqrt{\tau_{ii} + \frac{1-\beta}{\text{Ma}^2}})$ for each i, which means that the eigenvalues are real only when

$$\tau_{ii} + \frac{1-\beta}{\text{Ma}^2} > 0. \tag{15}$$

Following Tsai and Miller [20] for the Giesekus model, we get for the PTT model

$$\boldsymbol{G}\left(\boldsymbol{\tau}_p + \frac{1-\beta}{\text{Ma}^2}\right)\boldsymbol{G}^T = \int_{-\infty}^{t} e^{\frac{t-s}{\sqrt{\text{Ra}}\,\text{We}}}\left[\frac{1-\beta}{\sqrt{\text{Ra}}\,\text{We}\,\text{Ma}^2}\boldsymbol{G}\boldsymbol{G}^T \right.$$
$$\left. - \epsilon\frac{\sqrt{\text{Ra}}}{(1-\beta)\text{Pr}}\boldsymbol{G}\,\text{tr}(\boldsymbol{\tau}_p)\boldsymbol{\tau}_p\boldsymbol{G}^T - \xi\boldsymbol{G}(\boldsymbol{D}\boldsymbol{\tau}_p + \boldsymbol{\tau}_p\boldsymbol{D})\boldsymbol{G}^T\right]ds, \tag{16}$$

where $\boldsymbol{G}$ is the decomposition transformation gradient. The hyperbolicity of the PTT model requires that the RHS of Eq. (16) is positive,

$$\frac{1-\beta}{\sqrt{\text{Ra}}\,\text{We}\,\text{Ma}^2}\boldsymbol{G}\boldsymbol{G}^T - \epsilon\frac{\sqrt{\text{Ra}}}{(1-\beta)\text{Pr}}\boldsymbol{G}\,\text{tr}(\boldsymbol{\tau}_p)\boldsymbol{\tau}_p\boldsymbol{G}^T - \xi\boldsymbol{G}(\boldsymbol{D}\boldsymbol{\tau}_p + \boldsymbol{\tau}_p\boldsymbol{D})\boldsymbol{G}^T > 0. \tag{17}$$

This should be verified *a posteriori*.

If Eq. (17) holds true, we can rewrite A_i as $A_i = L_i\Lambda_i R_i$, where Λ_i is a diagonal matrix containing the eigenvalues of A_i. L_i is the matrix formed by the eigenvectors of A_i and R_i is the inverse of L_i. The convective terms in Eq. (12) at a fixed point can then be transformed into

$$A_i\frac{\partial W}{\partial x_i} = L_i\Lambda_i\frac{\partial R_i W}{\partial x_i}. \tag{18}$$

We note that at a fixed point L_i and R_i have constant coefficients and that R_i can be placed under partial differentiation in Eq. (18). This transformation allows us to calculate first $\Lambda_i \frac{\partial R_i W}{\partial x_i}$ by using suitable numerical schemes and to compute explicitly the convective terms $A_i \frac{\partial W}{\partial x_i}$ at any fixed point as can be seen hereafter.

B. Discretization and numerical method

The quasilinear formulation leads to the following governing system:

$$\frac{\partial T}{\partial t} + (\boldsymbol{u} \cdot \boldsymbol{\nabla})T = \frac{1}{\sqrt{\mathrm{Ra}}}\boldsymbol{\Delta} T,$$

$$\frac{\partial W}{\partial t} + \sum_{i=1}^{2} A_i \frac{\partial W}{\partial x_i} = S_{\mathrm{ql}},$$

$$\boldsymbol{\nabla} \cdot \boldsymbol{u} = 0. \tag{19}$$

It is discretized in time by a semi-implicit second-order scheme. Partial derivatives in time are treated by a second-order backward differential formulation (BDF2); quasilinear terms, PTT-related nonlinear terms, and the convective term in the energy equation are treated explicitly by a second-order extrapolation in time. Diffusion terms, relaxation terms, mass conservation, and pressure gradients are treated implicitly. Equation (19) discretized in time is then

$$\frac{3T^{(n+1)} - 4T^{(n)} + T^{(n-1)}}{2\Delta t} + 2[(\boldsymbol{u} \cdot \boldsymbol{\nabla})T]^{(n)} - [(\boldsymbol{u} \cdot \boldsymbol{\nabla})T]^{(n-1)} = \frac{1}{\sqrt{\mathrm{Ra}}}\boldsymbol{\Delta} T^{(n+1)},$$

$$\frac{3W^{(n+1)} - 4W^{(n)} + W^{(n-1)}}{2\Delta t} + 2\left(\sum_{i=1}^{2} A_i \frac{\partial W}{\partial x_i}\right)^{(n)} - \left(\sum_{i=1}^{2} A_i \frac{\partial W}{\partial x_i}\right)^{(n-1)} = S_{\mathrm{ql}}^{(n+1)},$$

$$\boldsymbol{\nabla} \cdot \boldsymbol{u}^{(n+1)} = 0, \tag{20}$$

with

$$S_{\mathrm{ql}}^{(n+1)} = \begin{bmatrix} -\boldsymbol{\nabla} p^{(n+1)} + \beta \frac{\mathrm{Pr}}{\sqrt{\mathrm{Ra}}}\boldsymbol{\Delta} \boldsymbol{u}^{(n+1)} + \mathrm{Pr}\, T^{(n+1)} e_j \\ \left(\frac{-\boldsymbol{\tau}_p^{(n+1)}}{\mathrm{We}\sqrt{\mathrm{Ra}}} - 2A\left[\frac{\epsilon\sqrt{\mathrm{Ra}}}{(1-\beta)\mathrm{Pr}}\mathrm{tr}(\boldsymbol{\tau}_p)\boldsymbol{\tau}_p + \xi(\boldsymbol{D}\boldsymbol{\tau}_p + \boldsymbol{\tau}_p\boldsymbol{D})\right]^{(n)} \right. \\ \left. +A\left[\frac{\epsilon\sqrt{\mathrm{Ra}}}{(1-\beta)\mathrm{Pr}}\mathrm{tr}(\boldsymbol{\tau}_p)\boldsymbol{\tau}_p + \xi(\boldsymbol{D}\boldsymbol{\tau}_p + \boldsymbol{\tau}_p\boldsymbol{D})\right]^{(n-1)}\right) \end{bmatrix}. \tag{21}$$

The above system is discretized on a uniform grid in space. All the unknowns are located at the cell corners except for the pressure located at the cell center. A second-order central differencing is applied to all the terms except for the quasilinear terms which are expressed by Eq. (18). A high-order (third-order) upstream central (HOUC-3) scheme [21] is applied to $\frac{\partial R_i W}{\partial x_i}$ according to the sign of the eigenvalues in Λ_i. For example, for $i = 1$ there are five eigenvalues $\lambda_1, \lambda_2, \dots, \lambda_5$ and five components of $R_1 W$ $[(R_1 W)^{(1)}, (R_1 W)^{(2)}, \dots, (R_1 W)^{(5)}]$. In order to calculate $\lambda_2 \frac{\partial (R_1 W)^{(2)}}{\partial x_1}$ at the grid point (l, m), the following HOUC-3 scheme is applied:

$$\lambda_2 \frac{\partial (R_1 W)^{(2)}}{\partial x_1}\bigg|_{l,m} = \begin{cases} \lambda_2 \frac{(R_1 W)_{l-2,m}^{(2)} - 6(R_1 W)_{l-1,m}^{(2)} + 3(R_1 W)_{l,m}^{(2)} + 2(R_1 W)_{l+1,m}^{(2)}}{6\Delta x_1} & \text{if } \lambda_2 > 0, \\ \lambda_2 \frac{-2(R_1 W)_{l-1,m}^{(2)} - 3(R_1 W)_{l,m}^{(2)} + 6(R_1 W)_{l+1,m}^{(2)} - (R_1 W)_{l+2,m}^{(2)}}{6\Delta x_1} & \text{if } \lambda_2 < 0, \\ 0 & \text{otherwise.} \end{cases} \tag{22}$$

Note that R_1 as $\lambda_1, \lambda_2, \dots, \lambda_5$ contains only information related to A_1 at the grid point (l, m) and that at any grid point (l, m) application of the HOUC-3 scheme to the five eigenvalues allows us to calculate $A_i \frac{\partial W}{\partial x_i}$ explicitly. Second-order schemes are used for grid points near the domain boundaries.

Equations (20) and (21), apart from the velocity-pressure coupling, lead to Helmholtz equations for the unknowns $T^{(n+1)}$, $u_1^{(n+1)}$, and $u_2^{(n+1)}$, and simple scalar equations for $\tau_{11}^{(n+1)}$, $\tau_{12}^{(n+1)}$, and $\tau_{22}^{(n+1)}$,

$$\left(1 + \frac{2\Delta t}{3\,\mathrm{We}\sqrt{\mathrm{Ra}}}\right)\tau_{ij}^{(n+1)} = \mathrm{RHS},\tag{23}$$

that can be easily solved at any grid point. We use the energy equation to illustrate the approach used to solve the Helmholtz equations. The method is similar to the alternative direction method. The Helmholtz equation for $T^{(n+1)}$ is written as

$$\left(1 - \frac{2\Delta t}{3\sqrt{\mathrm{Ra}}}\boldsymbol{\Delta}\right)T^{(n+1)} = \frac{4}{3}T^{(n)} - \frac{1}{3}T^{(n-1)} - \frac{4\Delta t}{3}[(\boldsymbol{u}\cdot\boldsymbol{\nabla})T]^{(n)} + \frac{2\Delta t}{3}[(\boldsymbol{u}\cdot\boldsymbol{\nabla})T]^{(n-1)}.\tag{24}$$

The 2D Helmholtz operator can be factorized into a product of two 1D operators:

$$1 - \frac{2\Delta t}{3\sqrt{\mathrm{Ra}}}\boldsymbol{\Delta} = \left(1 - \frac{2\Delta t}{3\sqrt{\mathrm{Ra}}}\frac{\partial^2}{\partial x_1^2}\right)\left(1 - \frac{2\Delta t}{3\sqrt{\mathrm{Ra}}}\frac{\partial^2}{\partial x_2^2}\right) - \frac{4\Delta t^2}{9\,\mathrm{Ra}}\frac{\partial^2}{\partial x_1^2}\frac{\partial^2}{\partial x_2^2}.\tag{25}$$

The cross term is of the order of Δt^2 and neglecting it results in a first-order time scheme. In order to keep a second-order time scheme, the factorized operator is only applied to the temperature increment $(T^{(n+1)} - T^{(n)})$ which is of the order of Δt. In this way

$$\frac{4\Delta t^2}{9\,\mathrm{Ra}}\frac{\partial^2}{\partial x_1^2}\frac{\partial^2}{\partial x_2^2}(T^{(n+1)} - T^{(n)})\tag{26}$$

becomes of the order of Δt^3 and can be neglected without decreasing the accuracy of the second-order time scheme. The final equation of temperature to be solved is the following:

$$\left(1 - \frac{2\Delta t}{3\sqrt{\mathrm{Ra}}}\frac{\partial^2}{\partial x_1^2}\right)\left(1 - \frac{2\Delta t}{3\sqrt{\mathrm{Ra}}}\frac{\partial^2}{\partial x_2^2}\right)(T^{(n+1)} - T^{(n)})$$
$$= \frac{2\Delta t}{3\sqrt{\mathrm{Ra}}}\boldsymbol{\Delta}T^{(n)} + \frac{1}{3}(T^{(n)} - T^{(n-1)}) - \frac{4\Delta t}{3}[(\boldsymbol{u}\cdot\boldsymbol{\nabla})T]^{(n)} + \frac{2\Delta t}{3}[(\boldsymbol{u}\cdot\boldsymbol{\nabla})T]^{(n-1)}.\tag{27}$$

The tridiagonal matrix algorithm (TDMA) is first applied in the x_1 direction and then in the x_2 direction to obtain the temperature increment. The same method is also used to solve the Helmholtz equations for the velocity.

The velocity-pressure coupling is treated by the projection method. Enforcing the incompressibility constraint at time step $(n + 1)$ in the momentum equation results in a Poisson equation for the pressure $p^{(n+1)}$ or its increment $(p^{(n+1)} - p^{(n)})$. The pressure increment is used in the present study. In the prediction step momentum equations are solved using the gradients of $p^{(n)}$. The resulting velocity field is not divergence free. In the correction step this velocity field is projected onto a divergence free space by using the gradients of $(p^{(n+1)} - p^{(n)})$ and the resulting Poisson equation is solved by a partial diagonalization method.

C. Numerical validation of the model

The intrinsic behavior of the numerical method was first tested. The results of the numerical tests confirmed that the code is second-order accurate both in time and space, in agreement with the theoretical behavior of the numerical schemes used in our previous work [22,23].

To validate that our solver has the ability to simulate the Rayleigh-Bénard convection with viscoelastic fluids, we consider a cavity of aspect ratio 2:1 filled with an Oldroyd-B type viscoelastic fluid heated from the bottom and cooled through the top. The parameters chosen for the validation purpose are $\beta = 0.2$, We $= 0.1$, and Pr $= 7.0$. $\beta = 0.2$ implies that the polymeric contribution is emphasized. For the same aspect ratio and the above parameters, Park and Ryu [14] reported an overstability or Hopf bifurcation leading to time-dependent flows. They also showed that for
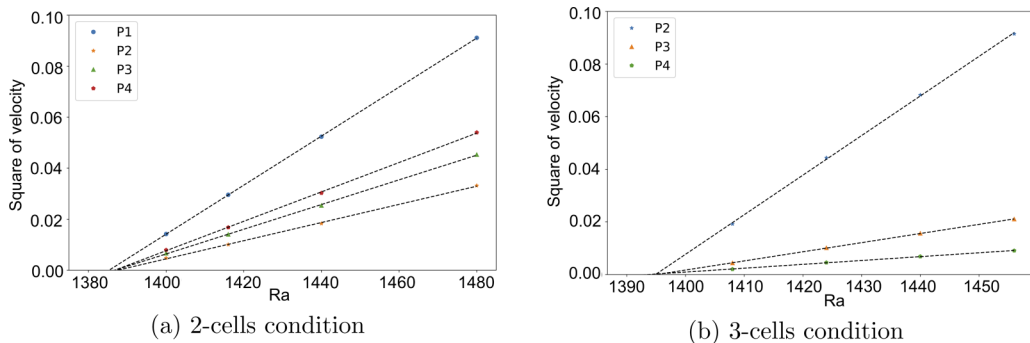
(a) 2-cells condition

(b) 3-cells condition

FIG. 2. Square of the amplitude of the vertical velocity at four monitoring points vs Ra in a 2 : 1 cavity filled with an Oldroyd-B fluid. (a) $\beta = 0.2$, We $= 0.1$, two-cell time-periodic flow (b) $\beta = 0.2$, We $= 0.1$, three-cell time-periodic flow. The monitoring points are P1 (1, 0.5), P2 (0.75, 0.5), P3 (0.25, 0.5), and P4 (0.5, 0.25). Spatial resolution used is 128×64. The solid lines are linear fitting curves of the numerical results and the linear relationship indicates that the corresponding bifurcation (Hopf bifurcation) is supercritical. The estimated Ra$_c$ is equal to 1387 (two-cell flow) and 1395 (three-cell flow).

the aspect ratio of 2 : 1 two modes with respectively two and three cells are unstable at almost the same Rayleigh number (about 1380). The simulations we performed for the aspect ratio 2 : 1 yield only a time-periodic flow of two cells. A three-cell time-periodic flow was first detected for the aspect ratio of 2.2 : 1 and then stabilized for the aspect ratio 2 : 1. We recall that due to the nondimensionalization adopted in this paper We $= 0.1$ corresponds to We $= 0.4$ in the paper of Park and Ryu [14]. Time-periodic flows were obtained for several supercritical Rayleigh numbers to calculate the corresponding critical Rayleigh numbers for both flow structures. The square of the velocity amplitudes versus Rayleigh number displays a linear relationship confirming that the convection mode transition takes place through a supercritical Hopf bifurcation [Figs. 2(a) and 2(b)]. Extrapolation of the linear relationship yields Ra$_c = 1387$ for the flow structure of two cells and Ra$_c = 1395$ for three flow cells. These critical Rayleigh numbers agree well with the results reported in Park and Lee [13].

The present results agree well with the previous study of viscoelastic RBC in the literature in terms of the flow structure (two or three cells), the flow feature (time dependent), and the critical Rayleigh number [14], thus validating the use of the present numerical approach to solve the viscoelastic RBC with fluids that obey the Oldroyd-B constitutive structure.

D. Grid independence verification

A study of the independence of the solver from grid resolution is required to have full confidence in the results of the numerical computations. The dimensionless time step is kept small enough $\delta t = 0.001$ in the verification process for the results not to be affected by the time step. Four grid resolutions were tested (122×56, 128×64, 144×72, 160×80). The square of the amplitude of the vertical velocity at monitoring point P1 as a function of Ra with all four grid resolutions is shown in Fig. 3. The critical Rayleigh numbers computed were 1386.4, 1386.8, 1387.0, and 1387.0, respectively. Clearly, the grid 128×64 is good enough to simulate cases in this paper as the Rayleigh numbers computed with grids with resolutions finer than 128×64 are not affected by the grid refinement.

IV. RESULTS AND DISCUSSION

A. Convection onset and critical Rayleigh number Ra$_{c1}$

The material parameters of the PTT model studied in this paper control the elongational response of the fluid, shear thinning, and the extent of the nonaffine motion. ϵ governs the elongational
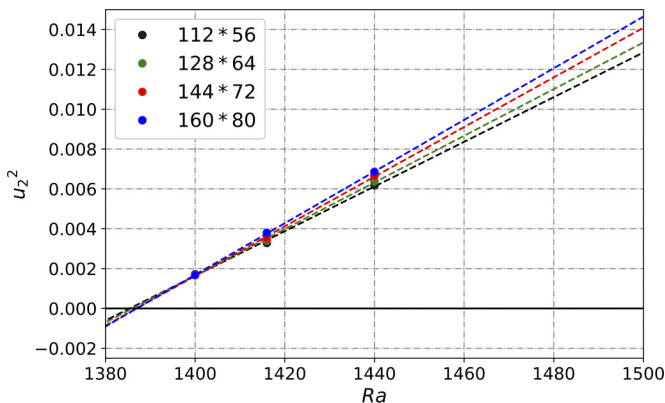
FIG. 3. Square of the amplitude of the vertical velocity at monitoring point P1 as function of Ra with four grid resolutions. The parameters used are Pr = 7.0, We = 0.1, $\beta = 0.2$, $\epsilon = 0.1$, and $\xi = 0.05$.

response and the shear thinning, while the parameter ξ controls the nonaffine movement of the molecular lattice relative to the flow of the solvent, quantifying the slip between the long chain molecules and the surrounding continuum. Simulations of two-cell flows have been conducted for various values of ξ with $\epsilon = 0.1$ and various values of ϵ with $\xi = 0$. These simulations aim to an understanding of their effects on the convection onset and heat transfer in flows of a wide range of viscoelastic fluids. The purpose in this paper is not to study a fixed fluid or industrial application, but to generally understand and quantify the effect of these constitutive parameters on the RBC. The rheological parameters of the PTT model, namely ϵ and ξ, come from experimental measurements. We note that the physical values of the material parameters depend on the type of working fluid. For example, dilute polymeric solutions such as low concentration polyethylene (LDPE) are characterized by $\epsilon = 0.02$ and $\xi = 0.1$, whereas concentrated polymeric solutions such as molten polyethylene (HDPE) are distinguished by $\epsilon = 0.02$, [24,25], or Shin *et al.* [26] who measured $\epsilon = 0.015$ and $\xi = 0.1$ for LDPE and $\xi = 0.7$ for HDPE. Other polymeric fluids, such as 5% polyisobutylene (PIB) solutions are characterized by $\epsilon = 0.25$ and $\xi = 0.25$ [27,28], or solutions of 2.5% polyisobutylene have $\epsilon = 0.42$, $\xi = 0.07$ [29].

The trends in the effects of the rheological parameters are important and should be determined as is sought after in this paper. We note that the numerical values of the material parameters depend not only on the specific working fluid but also on the structure of the constitutive equation adopted. The family of constitutive structures with the material parameters ξ is rather large [30]. An affine PTT or simplified phan thien tanner (SPTT) model is obtained when $\xi = 0$, and as for generalized Maxwell or the Giesekus models, a multimode version of the PTT model can be obtained by defining rheological parameters specific to each mode. If $\epsilon = 0$ and $\xi \neq 0$, the PTT model is reduced to the Johnson-Segalman model [30,31]. Hence, the Oldroyd-B model and upper convected Maxwell (UCM) model can be deduced from the PTT model with $\epsilon = 0$ and $\xi = 0$ and when $\epsilon = 0$, $\xi \neq 0$, and $\lambda = 0$ (relaxation time), the Newtonian behavior is obtained. In the light of the parametric analysis, we observe that ξ and ϵ have both a very weak influence on the convection onset and the critical Rayleigh number. With $\xi = 0$ and ϵ in the range of [0, 0.7] the critical Rayleigh number Ra_{c1} decreases slightly and remains almost constant thereafter. With $\epsilon = 0.1$ and ξ in the range of [0, 0.2] the decrease in Ra_{c1} is comparatively larger but still less than 2%. This means that an enhanced slip between polymer molecules and the surrounding continuum can make the onset of the oscillating convection occur slightly earlier.

For each pair of ξ and ϵ, several Rayleigh numbers are investigated. We find that convection onset takes place also with time-dependent flows. At supercritical Rayleigh numbers, the relationship between Ra and the square of the velocity amplitude is linear. This means that the corresponding
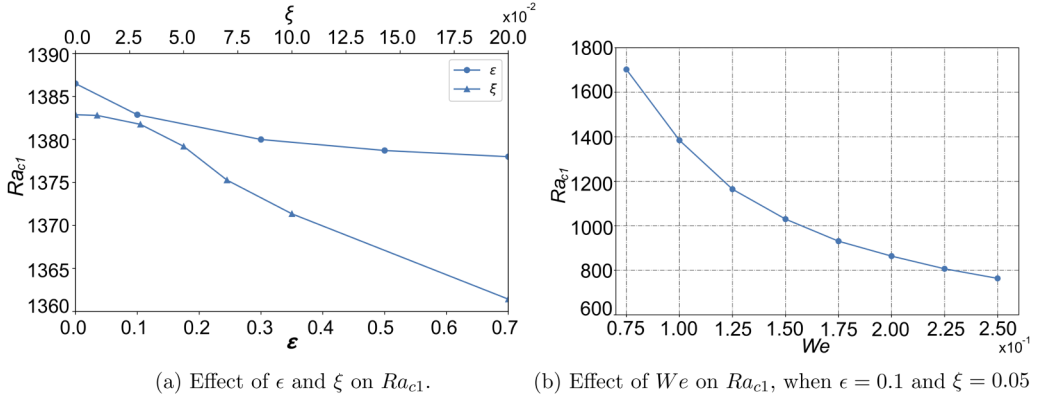
(a) Effect of ϵ and ξ on Ra_{c1}.

(b) Effect of We on Ra_{c1}, when $\epsilon = 0.1$ and $\xi = 0.05$

FIG. 4. Effects of ϵ, ξ, and We on the critical Rayleigh number of the two-cell flow pattern at Pr = 7.0, $\beta = 0.2$. In (a), the Weissenberg number is fixed at We = 0.1, and the effects of ϵ are studied for fixed $\xi = 0$ while those of ξ are investigated for $\epsilon = 0.1$. In (b), $\epsilon = 0.1$, $\xi = 0.05$.

Hopf bifurcation is supercritical. Through an extrapolation approach illustrated in Fig. 2, the corresponding critical Rayleigh number Ra_{c1} is determined and presented in Fig. 4(a).

The effect of We on the onset of RBC is also studied. Figure 4(b) depicts the behavior of Ra_{c1}, which decreases with increasing We. It decreases from $Ra_{c1} = 1700$ for We = 0.075 to $Ra_{c1} = 764$ for We = 0.25. It can be concluded therefore that among the parameters ϵ, ξ, and We, Ra_{c1} is more sensitive to We.

B. Flow pattern transition

Convective flow of two cells observed at $\epsilon = 0.1$, $\xi = 0.05$, and Ra = 1480 is chosen to better understand the flow pattern transition corresponding to the convection onset. We use the time evolution of the global kinetic energy defined by

$$E_{\text{Global}} = \int_{\Omega} \frac{1}{2}(u^2 + v^2)d\Omega, \tag{28}$$

where Ω is the computational domain. Figure 5 plots the global kinetic energy E_{Global} as a function of time and shows a regular periodic behavior, similar to that recently analyzed experimentally by Metivier *et al.* [32]. The present work on viscoelastic RBC is devoted to Pr = 7 due to the existing studies available in the literature. Experimentally speaking, most of the viscoelastic fluids are water
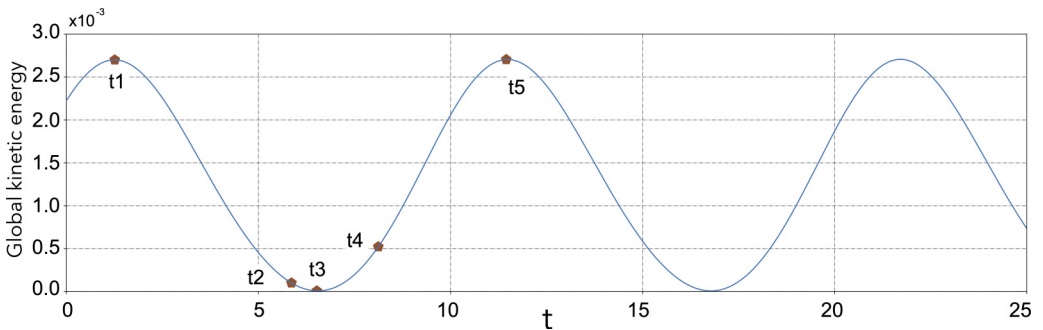

FIG. 5. Time evolution of global kinetic energy E_{Global} at five time points marked on the curve is studied in detail to show the flow pattern transition with $\epsilon = 0.1$, $\xi = 0.05$, $\beta = 0.2$, We = 0.1, and Ra = 1480.
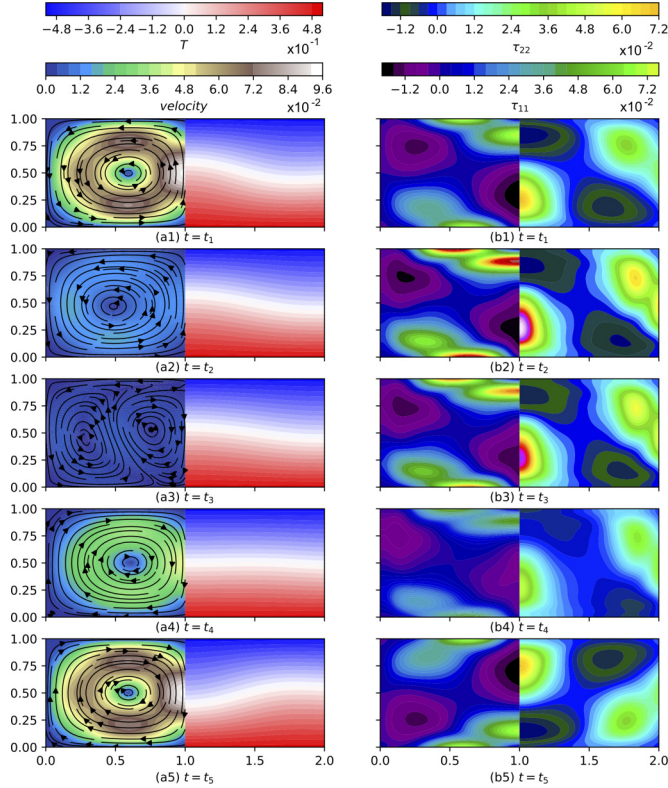
FIG. 6. Streamline and temperature (left) and extra-stress (right) snapshots of convection reversal in a 2:1 cavity filled with a PTT fluid ($\beta = 0.2$, We $= 0.1$, Pr $= 7.0$, $\epsilon = 0.1$, $\xi = 0.05$, and Ra $= 1480$) at the five time points indicated in Fig. 5. Streamlines are shown on the left side of each velocity module and the temperature field on the right side. The extra-stress component τ_{11} is shown on the left and component τ_{22} on the right of the column of figs.

solutions with polymers, surfactants, etc., and viscoelastic behavior is mainly due to increased viscosity compared to that of water while the corresponding thermal conductivity, specific heat, and density of the solutions remain to be more or less the same as water. In this sense most of the viscoelastic fluids have much higher Prandtl numbers. In order to experimentally check the existence of convection reversal observed in the present work and design experimental studies, it will be crucial to explore higher Prandtl number cases.

To our knowledge, an analysis of the Rayleigh-Bénard thermal convection with regard to the rheological characteristics is lacking except for the very recent work of Metivier *et al.* [32], who work with an elastoviscoplastic gel to investigate experimentally the transition from a two-cell structure to three-cell structure in the Rayleigh-Bénard convection. Determining the velocity vectors over a period of oscillation via experimental techniques, birefringence, and laser Doppler velocimetry, they demonstrate that elasticity plays a major role in the occurrence of the oscillations and that oscillations are in fact periodic traveling waves. This type of experimental bench will serve as a benchmark for numerical modeling validations and hence could give confidence in further numerical analysis and observations. In the present analysis, five points for half periods from t_1 to t_5 are marked in Fig. 5. Maximum kinetic energy is reached at t_1 and t_5 whereas t_3 is at the minimum kinetic energy (about zero). Note that one time period of kinetic energy is only one half of a time period of velocity. The flow fields corresponding to these five time points are displayed in Fig. 6. To clarify,
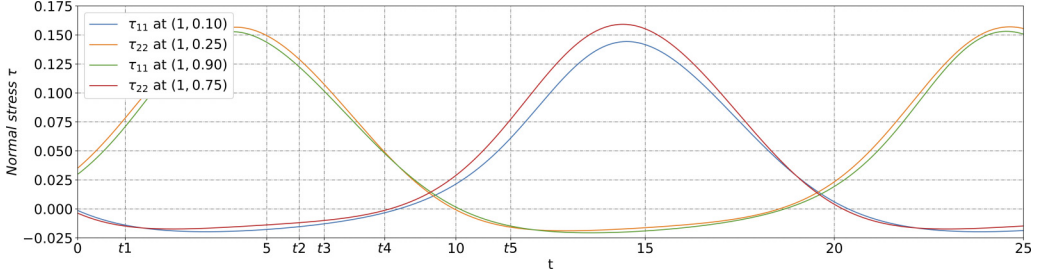
FIG. 7. Time evolution of the extra-stress components τ_{ii} at positions on the vertical centerline. It is clear from the evolution of these entities from t_1 to t_5 that the extrema of τ_{ii} occur later in time than the maximum of kinetic energy and therefore also later than the velocity extrema.

time evolutions of τ_{ii} at four points on the cavity midwidth are displayed in Fig. 7. It can be easily observed that there is a phase shift between E_{Global} and τ_{ii}.

At t_1, E_{Global} is maximum and flow is upward along the cavity centerline. The velocity gradient also reaches its extreme values. The extrema of the velocity gradient amplify and continue to amplify τ_{ij}. At t_2, the extrema of the τ_{11} and τ_{22} happen at about $(x, y) = (1, 0.9)$ and $(x, y) = (1, 0.3)$, respectively. These extrema are much larger than those in the same regions at t_1. From t_1 to t_2, the amplification of τ_{ij} also amplifies its divergence, for example, u_1 and u_2 are amplified due to $\frac{\partial \tau_{11}}{\partial x_1}$ and $\frac{\partial \tau_{22}}{\partial x_2}$, respectively. The increase in $\frac{\partial \tau_{11}}{\partial x_1}$ about $(x, y) = (0, 75, 0.9)$ increases u_1 there, and this makes u_1 (<0) evolve toward 0. The decrease in $\frac{\partial \tau_{22}}{\partial x_2}$ (<0) about $(x, y) = (1, 0.4)$ decreases u_2 there as well. The amplification of τ_{ij} weakens considerably the velocity field as the maximum velocity changes from approximately 0.09 at t_1 to approximately 0.015 at t_2. During the same period no significant change is observed on the temperature field. The weakening of the velocity field continues from t_2 to t_3 and t_4. At t_2 two small vortices appear near the bottom wall about the cavity vertical centerline, then grow rapidly up to t_3 to form a four-cell structure at t_3, and thereafter gradually merge and transit into a two-cell structure again in the cavity at t_4. It is in the interval from t_3 to t_4 that the temperature field undergoes an important evolution. At t_4 the temperature distribution is almost completely conductive. Note also that at t_4 the velocity field remains very weak and is downward along the cavity centerline. A weak velocity field means also a weak source term of $\boldsymbol{\tau_p}$. As $\boldsymbol{\tau_p}$ is governed approximately by

$$\frac{\partial \boldsymbol{\tau_p}}{\partial t} + \boldsymbol{\tau_p}/\text{We} + \frac{\epsilon \sqrt{\text{Ra}}}{(1-\beta)\text{Pr}} \text{tr}(\boldsymbol{\tau_p})\boldsymbol{\tau_p} = 0, \tag{29}$$

it is damped slightly from t_2 to t_3 and damped strongly from t_3 to t_4. The signs of τ_{11} and τ_{22} change along the vertical centerline on the way from t_4 to t_5. When t_4 is reached τ_{11} is positive at $(x, y) = (1, 0.8)$ and negative at $(x, y) = (1, 0.3)$, whereas at t_5, τ_{11} changes sign at the same locations and is negative at $(x, y) = (1, 0.8)$ and positive at $(x, y) = (1, 0.3)$. From t_4 to t_5 the velocity field is amplified to reach an extremum at t_5 and the temperature field also evolves from a conductive to convective distribution. Again the amplified velocity gradient amplifies $\boldsymbol{\tau_p}$ and the amplified extrema of $\boldsymbol{\tau_p}$'s divergence weaken the velocity field; a weak velocity field damps $\boldsymbol{\tau_p}$ in turn, small vortices appear near the top wall about the vertical centerline, grow rapidly and invade the cavity, flow direction is reversed, and the convective temperature distribution switches to a conductive distribution; the damping of $\boldsymbol{\tau_p}$ continues, τ_{ii} change signs along the cavity vertical centerline, velocity is amplified again to reach the extremum, and the temperature field becomes again convective.

The above observations indicate that there is a phase shift between the amplification and damping cycles of the velocity (Fig. 7) and the extra stress. This phase shift is responsible for the time-dependent flow regime.
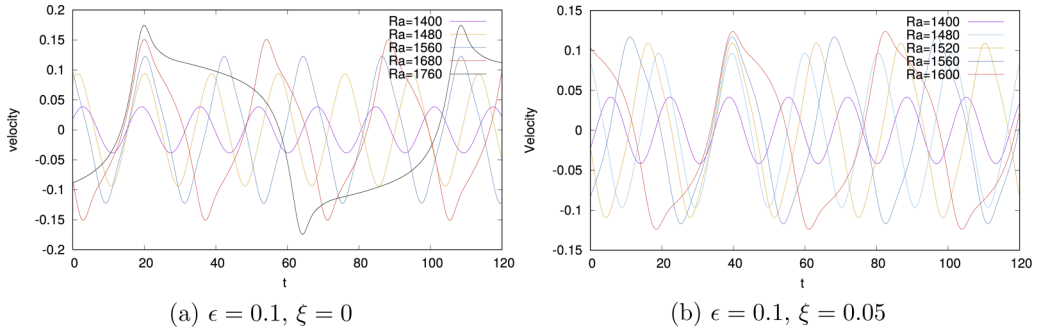
(a) $\epsilon = 0.1, \xi = 0$ (b) $\epsilon = 0.1, \xi = 0.05$

FIG. 8. Time evolution of u_2 at the cavity center $(x, y) = (1, 0.5)$. For both cases the amplitude and the frequency increase and decrease, respectively, with increasing Rayleigh number.

C. Steady-state flow at higher Ra

For fixed values of ϵ, ξ, and We, when increasing further the Rayleigh number, we observed that both the convection reversal period and the reversal amplitude increase with the Rayleigh number (Fig. 8). These figures show that with constant values of ϵ and We the increase of the slippage factor ξ increases the period of the velocity oscillations. That means the molecular slippage introduces a delay or reduction of the intensity and the frequency of the velocity oscillations and helps the stability of the system. Beyond a certain limit there is no more time-dependent flow and a steady-state flow is observed. This transition from time-periodic flow to steady-state flow corresponds to a drift pitchfork bifurcation not a Hopf bifurcation. In fact, the control parameter controlling the frequency of the reversal is equal to zero at the critical point. The oscillation frequency ω of the reversal convection flow is defined as $\omega = \frac{1}{q}$, where q is the oscillation period. Figure 9 displays the relationship between ω^2, the square of the oscillation frequency of the reversal convection flow, and the Rayleigh number. A trivial linear relationship is obvious. The drift pitchfork bifurcation is supercritical. The linear curve has a crossover point with $\omega^2 = 0$, which is the second bifurcation point, Ra_{c2}. An extrapolation of the linear fitting curve can be used again to obtain Ra_{c2}, the second critical Rayleigh number. Above Ra_{c2}, Rayleigh-Bénard convection flow is steady.

The same methodology is applied to $\epsilon \in [0.1, 0.7]$ with $\xi = 0$ and We $= 0.1$, $\xi \in [0.01, 0.2]$ with $\epsilon = 0.1$ and We $= 0.1$, and We $\in [0.075, 0.25]$ with $\epsilon = 0.1$ and $\xi = 0.05$, and the corresponding Ra_{c2} was obtained. Figure 10 plots two critical Rayleigh numbers Ra_{c1} and Ra_{c2} against different values of ϵ, ξ, and We used to illustrate their effects on the critical Rayleigh numbers. Ra_{c2}
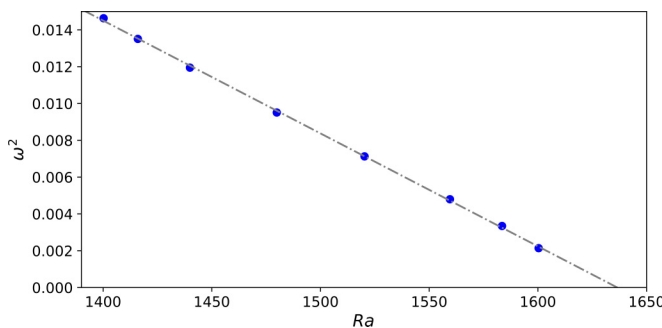

FIG. 9. Square of the oscillation frequency of reversal convection flow vs Rayleigh number ($\beta = 0.2$, We $= 0.1$, Pr $= 7.0$, $\epsilon = 0.1$, and $\xi = 0.05$). A linear relationship is observed and the extrapolation of the linear fitting line yields $Ra_{c2} = 1635$.
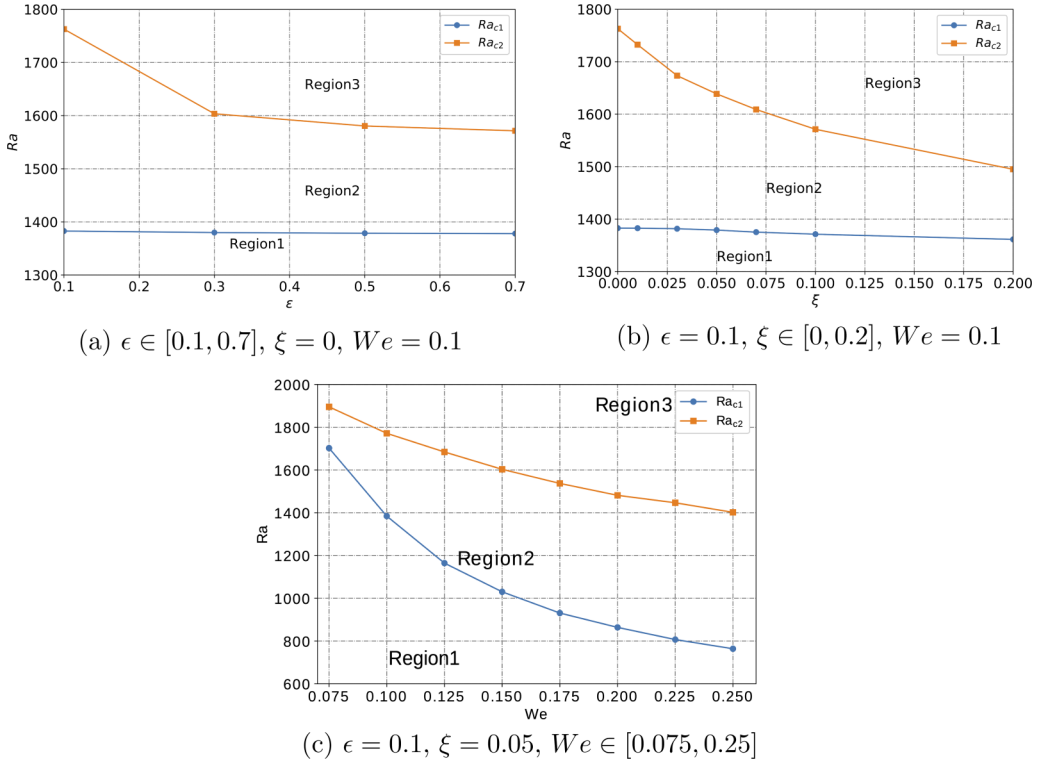
(a) $\epsilon \in [0.1, 0.7]$, $\xi = 0$, $We = 0.1$

(b) $\epsilon = 0.1$, $\xi \in [0, 0.2]$, $We = 0.1$

(c) $\epsilon = 0.1$, $\xi = 0.05$, $We \in [0.075, 0.25]$

FIG. 10. Critical Rayleigh numbers Ra_{c1} and Ra_{c2} vs ϵ and ξ. (a) Effect of the ϵ on Ra_c with $\xi = 0$ and $We = 0.1$. (b) Effect of ξ on Ra_c with $\epsilon = 0.1$ and $We = 0.1$. (c) Effect of We on Ra_c with $\epsilon = 0.1$ and $\xi = 0.05$. The critical Rayleigh numbers Ra_{c1} and Ra_{c2} divide the flow regime into three regions: pure conduction without convective flow (region 1), time-periodic convective flow bounded by Ra_{c1} and Ra_{c2} (region 2), and steady-state convective flow for $\mathrm{Ra} > \mathrm{Ra}_{c2}$ (region 3).

decreases with increasing ϵ (with $\xi = 0$ and $We = 0.1$) and ξ (with $\epsilon = 0.1$ and $We = 0.1$). The decrease in Ra_{c2} is more pronounced than that in Ra_{c1}. Ra_{c2} decreases from 1762 at $\epsilon = 0.1$ to 1585 at $\epsilon = 0.7$ for $\xi = 0$ and $We = 0.1$ and from 1732 at $\xi = 0.01$ to 1500 at $\xi = 0.2$ with $\epsilon = 0.1$ and $We = 0.1$. We note that the impact of the slippage parameter ξ is higher than that of the elongation related parameter ϵ [Figs. 10(a) and 10(b)]. Similarly, Ra_{c2} decreases with increasing We ($\epsilon = 0.1$ and $\xi = 0.05$). The influence of We on Ra_{c2} slightly supersedes those of ϵ and ξ. This means that the elasticity of the fluid, represented by the Weissenberg number, tends to make the transition to the steady-state flow to occur at lower critical Rayleigh number Ra_{c2}. Two critical Rayleigh numbers separate the studied domain into three regions in terms of flow and heat transfer. In Fig. 10(b): (i) pure heat conduction without convection flow, $\mathrm{Ra} < \mathrm{Ra}_{c1}$ (region 1); (ii) time-periodic oscillating flow, $\mathrm{Ra}_{c1} < \mathrm{Ra} < \mathrm{Ra}_{c2}$ (region 2); (iii) steady-state convective flow and heat transfer, $\mathrm{Ra} > \mathrm{Ra}_{c2}$ (region 3). Note that region 2 decreases with increasing ϵ and ξ due to the decrease of Ra_{c2}. Despite the fact that both Ra_{c1} and Ra_{c2} decrease with We, region 2 becomes bigger with increasing We. This enlargement of region 2 is essentially due to the decrease of Ra_{c1}, i.e., transition from a pure conduction to convection regime, suggesting that elasticity tends to quicken the transition ($\mathrm{Ra}_{c1} = 800$), but its effect on the stabilization of the flow to reach the steady state, via the decrease of the Ra_{c2}, is less pronounced in the range of the Weissenberg numbers investigated. In other words, this means that at small We, time-dependent flows exist only for a small range of the Rayleigh number. However, for higher We, time-dependent flows take place for a larger range of Ra. The steady-state flow regime in region 3 (above Ra_{c2}) is not investigated in the present paper.

D. Heat transfer

To study heat transfer and the influence of the material parameters, we define the spatially averaged Nusselt number Nu_s and the Nusselt number averaged in time and space Nu_{ts}:

$$\mathrm{Nu}_s = \frac{1}{2} \int_0^2 \left. \frac{\partial T}{\partial y} \right|_{y=0} dx,$$

$$\mathrm{Nu}_{ts} = \frac{1}{\lambda} \frac{1}{2} \int_0^\lambda \int_0^2 \left. \frac{\partial T}{\partial y} \right|_{y=0} dx dt.$$

To investigate the effects of ϵ and ξ on heat transfer, two pairs of (ϵ, ξ), $(0.1, 0)$ and $(0.1, 0.05)$, are chosen, several Rayleigh numbers are studied, and the corresponding Nusselt numbers are displayed in Fig. 11. The time evolution of the spatially averaged Nusselt number Nu_s is shown for the Rayleigh numbers investigated in Figs. 11(a) and 11(b). For a fixed pair of (ϵ, ξ), both the amplitude and the period of Nu_s increase with increasing Rayleigh numbers in the same way as the velocity. It is worth mentioning that the frequency of Nu_s is twice that of the velocity. One time period of velocity is twice that of Nu_s and there are two maximum values and two minimum values of Nu_s in one velocity period.

When velocity gets to its maximum value, Nu_s reaches the first maximum value [instantaneous local Nu distribution is shown in Figs. 11(c) and 11(d) and maximum Nu takes place near the two vertical walls]; then convection reversal occurs, velocity drops from maximum to zero, and Nu_s moves from the first maximum to the first minimum value of about one. Subsequently, velocity continues the decrease to reach its minimum value and fluid moves in the opposite direction, and at the same time Nu_s reaches the second maximum value [local Nu on the bottom wall is depicted in Figs. 11(e) and 11(f) and maximum Nu locates at the cavity midwidth].

To illustrate clearly the effect of the fluid parameters ϵ and ξ on the heat transfer, Figs. 12(a) and 12(b) present the evolution of the Nusselt number averaged in time and space Nu_{ts} vs Ra for different values of (ϵ, ξ). These figures are to be analyzed in the light of Fig. 10. In fact, we can note that, due to the reduction of region 2 with increasing ϵ and ξ, Nu curves are shorter for large ϵ and ξ.

We find that for $\xi = 0$, increasing ϵ decreases Nu_{ts}, and that for $\epsilon = 0.1$, increasing ξ increases Nu_{ts} slightly. ϵ and ξ have opposite but limited effects on heat transfer. In other words, increasing elongational behavior of polymer molecules decreases slightly the heat transfer in the time-dependent flow regime, but the slip parameter ξ enhances a bit the heat transfer. The influence of the We on the Nu_{ts} under different Ra with $\beta = 0.2$, $\epsilon = 0.1$, and $\xi = 0.05$ is also investigated [Fig. 12(c)]. As in Fig. 9, this figure shows that when increasing We the Nu_{ts} curves become longer due to a larger region 2 and shift to smaller Ra due to the decrease of Ra_{c1}. Clearly it shows the high impact of the elasticity on the transition from the conduction regime to the convection-conduction one, and hence increases the Nusselt number. It can be seen that at the same Ra, the increase of We, i.e., the increase of elasticity, will enhance heat transfer. Compared with ϵ and ξ, We has a stronger and more beneficial influence on Nu_{ts}.

V. CONCLUSION

A two-dimensional numerical simulation of laminar convection in a rectangular enclosure filled with a nonlinear viscoelastic fluid and heated from the bottom is performed in the present study.

In the case of an Oldroyd-B fluid, with increasing Weissenberg number and decreasing viscosity ratio β, a time-dependent flow, instead of a steady flow, exists at the convection onset. Time-dependent convection onset in an enclosure of aspect ratio 2:1 is chosen to validate the code developed using the parameters $\beta = 0.2$, We $= 0.1$, and Pr $= 7$. Critical Rayleigh numbers are obtained and compared with those in the literature for these values of the parameters for both

(a) $\epsilon = 0.1$, $\xi = 0$

(b) $\epsilon = 0.1$, $\xi = 0.05$

(c) $\epsilon = 0.1$, $\xi = 0$, at $t = t_1$

(d) $\epsilon = 0.1$, $\xi = 0.05$, at $t = t_1$

(e) $\epsilon = 0.1$, $\xi = 0$, at $t = t_5$
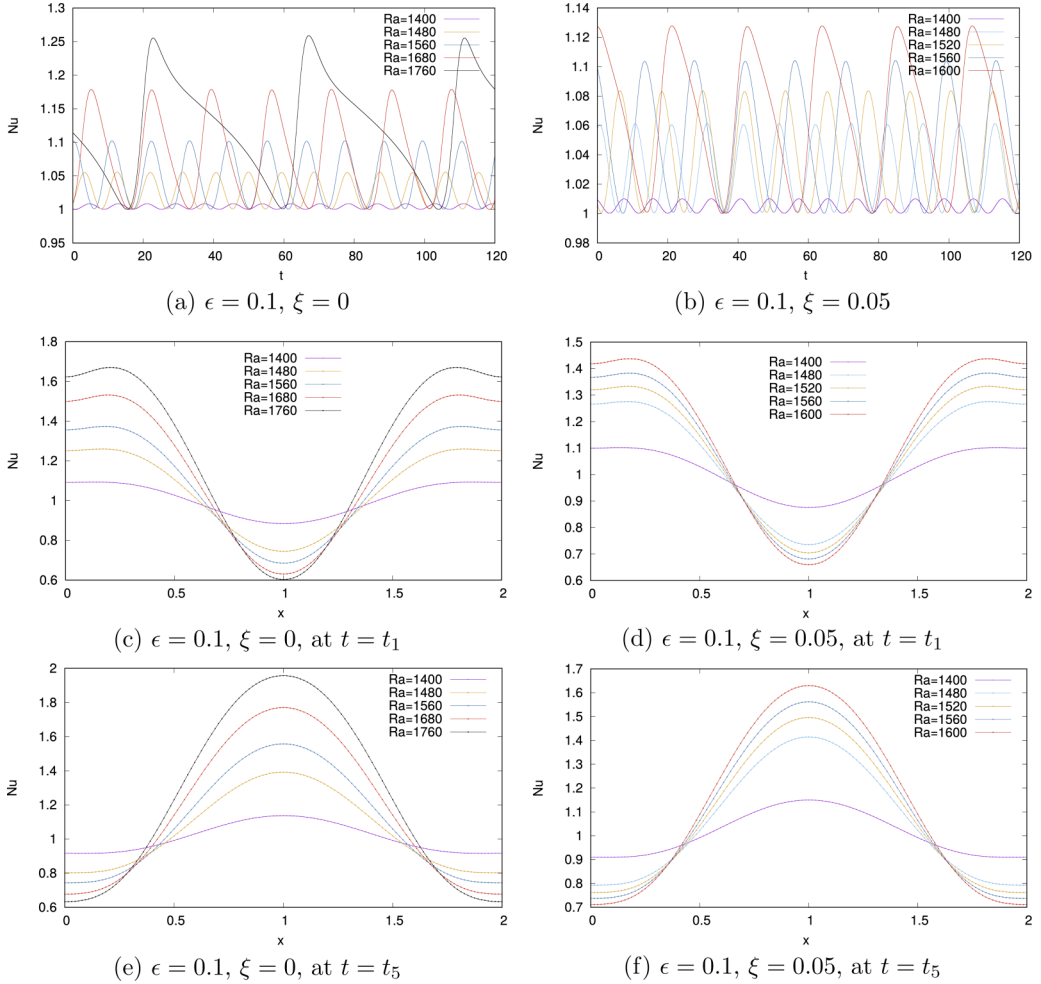
(f) $\epsilon = 0.1$, $\xi = 0.05$, at $t = t_5$

FIG. 11. Time evolution of Nu_s [(a) and (b)] and instantaneous local Nu on the bottom wall [(c)–(f)] at different Ra for two-cell convective flow. (c) and (d) correspond to the time point t_1 while (e) and (f) to the time point t_5. Both t_1 and t_5 concern the maximum of the global kinetic energy: At t_1 upward convective flow near the cavity center is at its maximum and the minimum of Nu on the bottom wall is located at $x = 1$; at t_5 downward convective flow near the cavity center is at its maximum and the maximum of Nu on the bottom wall is located at $x = 1$.

two-cell and three-cell convection flow configurations: The good agreement obtained thus validates the code developed.

Critical Rayleigh numbers corresponding to the onset of time-dependent convection, Ra_{c1}, are determined for various values of the constitutive parameter ϵ with $\xi = 0$ and We $= 0.1$ and various values of the constitutive parameter ξ with fixed $\epsilon = 0.1$ and We $= 0.1$. There is only a slight dependency of the critical Rayleigh number on these parameters. A similar study conducted with $\epsilon = 0.1$ and $\xi = 0.05$ reveals that Ra_{c1} decreases with increasing We and that the influence of We on Ra_{c1} is more significant. A two-cell flow structure is investigated in detail. We determine that the phase shift between the periodic cycles of the velocity and the extra stress is responsible for the time-dependent flow. At higher Rayleigh numbers, time-dependent flow is replaced by a steady-state flow. This flow transition corresponds to a drift pitchfork bifurcation. The critical Rayleigh
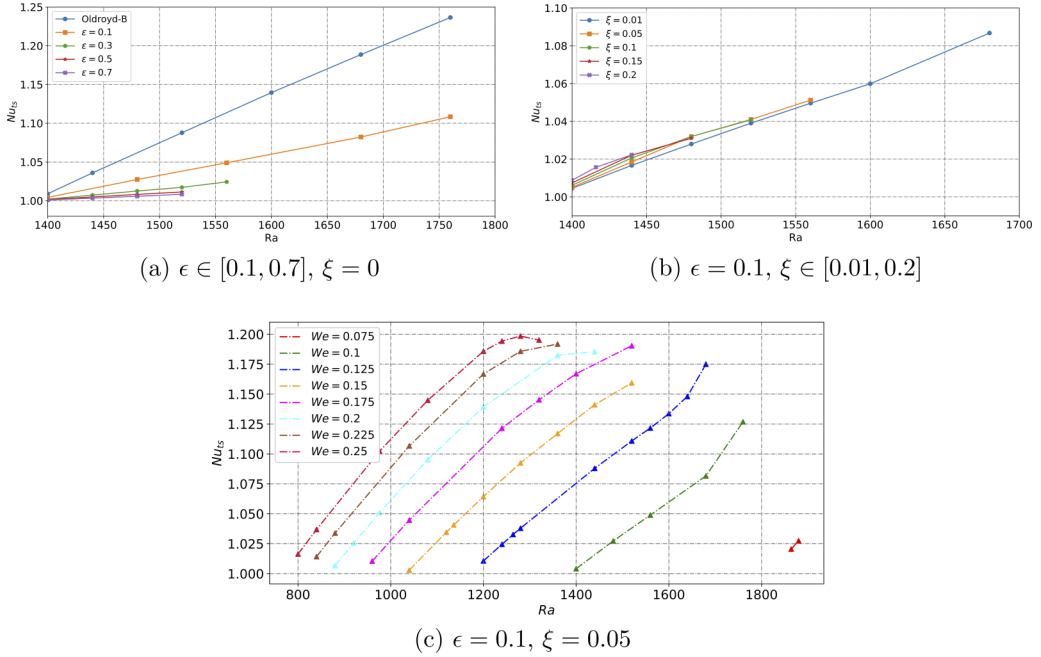
FIG. 12. (a) Effects of ϵ on the Nusselt number averaged in time and space Nu_{ts} of two-cell convection flow at $Pr = 7.0$, $\beta = 0.2$, $\xi = 0$, and $We = 0.1$. Increasing ϵ decreases Nu_{ts}. (b) With $Pr = 7.0$, $\beta = 0.2$, $\epsilon = 0.1$, and $We = 0.1$, increasing ξ only slightly increases Nu_{ts}. (c) With $Pr = 7.0$, $\beta = 0.2$, $\epsilon = 0.1$, and $\xi = 0.05$, higher We leads to higher Nu_{ts} at the same Rayleigh number. Note that the reduced range of Ra at higher ϵ and ξ corresponds to the fact that Ra_{c2} is reduced at higher ϵ and ξ (the Ra range of the time-dependent flow is reduced).

number Ra_{c2} is also determined for various values of ϵ with $\xi = 0$ and $We = 0.1$, various values of ξ with $\epsilon = 0.1$ and $We = 0.1$, and various values of We with $\epsilon = 0.1$ and $\xi = 0.05$. For the parameters investigated, all the three parameters, ξ, ϵ, and We, have an important influence on Ra_{c2}, and furthermore, Ra_{c2} decreases with the increase of the three parameters.

The influence of ϵ and ξ on heat transfer is investigated for the time-dependent flow regime. ϵ and ξ have opposite but limited effects on heat transfer. Increasing ϵ decreases the Nusselt number whereas the Nusselt number increases slightly with increasing ξ. The impact of We on heat transfer is also studied for the time-dependent flow regime with $Pr = 7.0$, $\beta = 0.2$, $\epsilon = 0.1$, and $\xi = 0.05$, and increasing We increases Nu_{ts} was found for a fixed Rayleigh number.

The onset of the time-dependent convection in the Rayleigh-Bénard convection with nonlinear viscoelastic fluids is an interesting flow feature because of the particular flow patterns and flow reversal. These flow reversal characteristics should be distinguished from random reversal in turbulent Rayleigh-Bénard convection.

ACKNOWLEDGMENT

---

[1] H. Park and D. Ryu, Nonlinear convective stability problems of viscoelastic fluids in finite domains, Rheol. Acta **41**, 427 (2002).

[2] S. Chandrasekhar, *Hydrodynamic and Hydromagnetic Stability* (Courier Corporation, North Chelmsford, MA, 2013).

[3] W. Malkus and G. Veronis, Finite amplitude cellular convection, J. Fluid Mech. **4**, 225 (1958).

[4] T. Green III, Oscillating convection in an elasticoviscous liquid, Phys. Fluids **11**, 1410 (1968).

[5] C. M. Vest and V. S. Arpaci, Overstability of a viscoelastic fluid layer heated from below, J. Fluid Mech. **36**, 613 (1969).

[6] M. Sokolov and R. Tanner, Convective stability of a general viscoelastic fluid heated from below, Phys. Fluids **15**, 534 (1972).

[7] I. A. Eltayeb, Nonlinear thermal convection in an elasticoviscous layer heated from below, Proc. R. Soc. London, Ser. A **356**, 161 (1977).

[8] S. Rosenblat, Thermal convection in a viscoelastic liquid, J. Non-Newtonian Fluid Mech. **21**, 201 (1986).

[9] M. Renardy and Y. Renardy, Pattern selection in the Bénard problem for a viscoelastic fluid, Z. Angew Math. Phys. **43**, 154 (1992).

[10] J. Martinez-Mardones and C. Perez-Garcia, Linear instability in viscoelastic fluid convection, J. Phys.: Condens. Matter **2**, 1281 (1990).

[11] J. Martinez-Mardones and C. Perez-Garcia, Bifurcation analysis and amplitude equations for viscoelastic convective fluids, Nuovo Cimento D **14**, 961 (1992).

[12] H. Park and H. Lee, Nonlinear hydrodynamic stability of viscoelastic fluids heated from below, J. Non-Newtonian Fluid Mech. **60**, 1 (1995).

[13] H. Park and H. Lee, Hopf bifurcations of viscoelastic fluids heated from below, J. Non-Newtonian Fluid Mech. **66**, 1 (1996).

[14] H. Park and D. Ryu, Rayleigh-Bénard convection of viscoelastic fluids in finite domains, J. Non-Newtonian Fluid Mech. **98**, 169 (2001).

[15] H. Park and K. Park, Rayleigh-Bénard convection of viscoelastic fluids in arbitrary finite domains, Int. J. Heat Mass Transfer **47**, 2251 (2004).

[16] H. Park, Peculiarity in the Rayleigh-Bénard convection of viscoelastic fluids, Int. J. Therm. Sci. **132**, 34 (2018).

[17] J.-P. Cheng, H.-N. Zhang, W.-H. Cai, S.-N. Li, and F.-C. Li, Effect of polymer additives on heat transport and large-scale circulation in turbulent Rayleigh-Bénard convection, Phys. Rev. E **96**, 013111 (2017).

[18] M. J. Crochet, A. R. Davies, and K. Walters, *Numerical Simulation of Non-Newtonian Flow* (Elsevier, Amsterdam, 2012).

[19] D. Trebotich, P. Colella, and G. Miller, A stable and convergent scheme for viscoelastic flow in contraction channels, J. Comput. Phys. **205**, 315 (2005).

[20] W.-C. Tsai and G. H. Miller, Numerical simulations of viscoelastic flow in complex geometries using a multi-mode Giesekus model, J. Non-Newtonian Fluid Mech. **210**, 29 (2014).

[21] R. R. Nourgaliev and T. G. Theofanous, High-fidelity interface tracking in compressible flows: Unlimited anchored adaptive level set, J. Comput. Phys. **224**, 836 (2007).

[22] F. Hagani, M. Boutaous, R. Knikker, S. Xin, and D. Siginer, Numerical modeling of phan-thien-tanner viscoelastic fluid flow through a square cross-section duct: Heat transfer enhancement due to shear-thinning effects, in *ASME International Mechanical Engineering Congress and Exposition*, Vol. 52101 (American Society of Mechanical Engineers, New York, 2018), p. V007T09A042.

[23] X. Zheng, M. Boutaous, S. Xin, D. A. Siginer, F. Hagani, and R. Knikker, A new approach to the numerical modeling of the viscoelastic Rayleigh-Benard convection, in *ASME International Mechanical Engineering Congress and Exposition*, Vol. 59445 (American Society of Mechanical Engineers, New York, 2019), p. V007T08A027.

[24] R. G. Larson, *Constitutive Equations for Polymer Melts and Solutions: Butterworths Series in Chemical Engineering* (Butterworth-Heinemann, Oxford, UK, 2013).

[25] C. Carrot, J. Guillet, P. Revenu, and A. Arsac, *Experimental Validation of Nonlinear Network Models*, Rheology Series, Vol. 5 (Elsevier, Amsterdam, 1996), pp. 141–198.

[26] D. M. Shin, J. S. Lee, J. M. Kim, H. W. Jung, and J. C. Hyun, Transient and steady-state solutions of 2D viscoelastic nonisothermal simulation model of film casting process via finite element method, J. Rheol. **51**, 393 (2007).

[27] L. M. Quinzani, R. C. Armstrong, and R. A. Brown, Birefringence and laser-Doppler velocimetry (LDV) studies of viscoelastic flow through a planar contraction, J. Non-Newtonian Fluid Mech. **52**, 1 (1994).

[28] J. Azaiez, R. Guenette, and A. Ait-Kadi, Entry flow calculations using multi-mode models, J. Non-Newtonian Fluid Mech. **66**, 271 (1996).

[29] J. F. Schoonen, F. H. Swartjes, G. W. Peters, F. Baaijens, and H. E. Meijer, A 3D numerical/experimental study on a stagnation flow of a polyisobutylene solution, J. Non-Newtonian Fluid Mech. **79**, 529 (1998).

[30] D. A. Siginer, *Developments in the Flow of Complex Fluids in Tubes* (Springer, Berlin, 2015).

[31] M. Johnson and D. Segalman, A model for viscoelastic fluid behavior which allows non-affine deformation, J. Non-Newtonian Fluid Mech. **2**, 255 (1977).

[32] C. Metivier, F. Brochard, M. Darbouli, and A. Magnin, Oscillatory Rayleigh-Bénard convection in elasto-viscoplastic gels, J. Non-Newtonian Fluid Mech. **286**, 104428 (2020).